Agglomeration of particles by a converging ultrasound field and their quantitative assessments

Tianquan Tang [a,b,*], Bin Dong [a,b], Lixi Huang [a,b]

[a] *Department of Mechanical Engineering, The University of Hong Kong, Pokfulam, Hong Kong SAR, China*
[b] *Lab for Aerodynamics and Acoustics, HKU Zhejiang Institute of Research and Innovation, 1623 Dayuan Road, Lin An District, Hangzhou, China*

ARTICLE INFO

ABSTRACT

The acoustic radiation force resulting from acoustic waves have been extensively studied for the contact-free generation of organized patterning arrays. The precise arrangement of microscopic objects clustered at the pressure nodes is critical to the development of functional structures and patterned surfaces. However, the size of the clusters is restricted by the saturation limit of the acoustic nodes. Here, we present a bulk acoustic wave (BAW) platform, which employs a two-dimensional acoustic wave to propel particles of various sizes. Experimentally, when particles are large, significant acoustic energy is scattered and partly absorbed by the matched layers in front of the sensors. The acoustic radiation force from a convergent acoustic pressure field agglomerates the large polystyrene (PS) particles towards the central region instead of the pressure nodes. The parametric analysis has been performed to assess the transition in the particles from clustering at the organized nodal arrays to agglomerating in the central region, which is a function of particle size, particle concentration, and load voltage. Statistically, the particles can agglomerate with a cluster ratio greater than 70%, and this ratio can be improved by increasing the load power/voltage supplied to the transducers. With its ability to perform biocompatible, label-free, and contact-free self-assembly, this concept offers a new possibility in the fabrication of colloidal layers, the recreation of tissue microstructure, the development of organoid spheroid cultures, the migration of microorganisms, and the assembly of bioprinting materials.

1. Introduction

The self-assembly of individual microparticles is essential for the fields of separations [1,2], printing [3], trapping [4], and imaging [5–7]. External magnetic [8] and optical [9] manipulations have been used to spatially control and facilitate the self-assembly process and provide precise manipulation over particle motions. However, the magnetic techniques require particles with magnetically susceptible properties, and the optical methods are limited by sample damage due to extensive heating by lasers [10]. Recently, acoustic patterning with ultrasound standing waves has emerged as a potent alternative for the formation of desirable structures [11,12], with the benefit that manipulation is not restrained by the properties of the material and the suspension media. In this approach, particle/cell can be rapidly and dynamically patterned using the bulk acoustic waves (BAW) or surface acoustic waves (SAW) within the suspension medium; characteristics that make this technique highly suited to generating complex patterns and motions [13–15].

In theory, the acoustic patterns are resulting from the acoustic

radiation forces acting on the particle populations; the driving force is a second-order effect caused by nonlinearities in physics [16]. Conveniently, Gor'kov derived the time-averaged acoustic radiation force acting on the microparticles using a potential field, where the spatial gradient gives the exerted force [17]. In the BAW and SAW fields, a set of potential wells are provided by ultrasound standing waves. In these conditions, acoustic force traps the microparticles into the wells.

To date, acoustic waves have been widely used in the manipulation of micro-objects and their self-assembly. Owens *et al.* [18] employed two lead zirconate titanate (PZT) transducers to generate standing bulk waves inside a reflective microchamber. As the microparticles differ in density or compressibility from the surrounding medium, the time-averaged acoustic radiation force propels particles with a density greater/smaller than the host medium towards the pressure nodes/anti-nodes in the two-dimensional plane. The microparticles with different natural properties were separated in a batch process. Similarly, Ate-hortua *et al.* [19] demonstrated a method of utilizing the PZT transducers to generate the standing waves inside a square tube to cluster the

---

water droplets from the water/oil emulsion at the pressure nodes. In this method, they successfully made the small water droplets coalesce into bigger ones at the acoustic pressure nodes, improving the efficiency in separating the water and the crude oil in the separator vessel. Additionally, the promise of this approach has inspired a wealth of research for organizing cell populations [20,21] and recreating tissue structures [22,23] in the biochemical industry.

However, the size of the self-assembly clusters formed at the acoustic pressure nodes with this approach is restricted by the saturation limit of the pressure nodes. A potential alternative is to introduce a fluidic flow. The particles/cells are first assembled at the pressure nodes of the standing wave. Then, the flow continuously transports the microparticles/cells to the trapping zone and the assembled crystal to the downstream region. Consequently, the microparticles/cells are able to cluster and form the single- or even multiple-layer colloidal structures [24,25]. In practice, introducing the acoustofluidic flow to transport the saturated crystals or the assembled micro-objects is not always controllable and desirable. It requires an experiential selection of the flow rate and an exquisite design of the microfluidic channel for a specific assembled layer or structure. In the BAW cavity with two orthogonal pairs of transducers [26], the extent of patterning of microparticles (Rayleigh regime $ka \ll 1$, where k and a are respectively the wavenumber and radius of the microparticles) is mainly dependent on the acoustic radiation force, which is solely decided by the load voltages and excitation frequencies of the ultrasound transducers [27]. However, in manipulating large particles beyond the Rayleigh regime, the ultrasound attenuation due to scattering should be considered [28]. The pressure field converges to the central region rather than the well-defined arrays due to the acoustic attenuation from scattering. In other words, the acoustic force would agglomerate the particles towards the central domain, regardless of the saturation limit. As a result, this assembly mechanism represents an advance in the technique for forming the single- and multiple-layer crystalline structures, recreating the two-dimensional cellular tissue, and isolating the objects of different sizes in various medium.

Here, we demonstrate the conditions that the particles concentrate towards the center in a BAW platform. Quantification assessment and parametric analysis of the particle agglomeration are performed with the help of Voronoï tessellation technique [29], which allows us to compare the products in an impartial and statistical manner across different experimental conditions. The experimental platform comprises four piezoceramic plates affixed to the inner walls of the cuboid cavity. The BAWs from the piezoceramic plates result in the acoustic radiation force that moves the particles. The scattered waves transfer acoustic energy to the matched layers affixed to the front face of the piezoceramic plates, where the scattered power is absorbed. In this approach, the gradient of acoustic intensity leads to a convergent Gor'kov potential field, thereby giving rise to a directional acoustic radiation force. The force drives the particles towards the center of the BAW platform. Experiments have been first performed across a wide range of various parametric combinations (such as size parameters, weight percentages, and load voltages) to make the particles cluster as the well-defined cluster arrays (the regular grid patterns) or agglomerate together. Then, Voronoï tessellation maps are used to evaluate the particle agglomeration in different experimental conditions. In this case, we statistically conclude the necessary conditions and parametric boundaries to establish the agglomeration results.

2. Methods

2.1. Theoretical models

Recently, acoustic patterning with ultrasound standing waves has emerged as a powerful technology for manipulating spatially inorganic micro-objects and organizing cell populations [14,19–21]. The physical mechanism is that the position-dependent Gor'kov potential results in a time-averaged acoustic radiation force, which moves the objects towards the potential wells [30].

2.1.1. The acoustic force

For the host fluid with the density of ρ_0 and the speed of sound of c_0, the acoustic radiation force, $\overrightarrow{F}_{\mathrm{rad}}$, resulting from the Gor'kov potential, U, can be calculated as [17]:

$$\overrightarrow{F}_{\mathrm{rad}} = -\nabla U. \tag{1}$$

The magnitude of the potential is given by

$$U = 2\pi a^3 \left[\frac{1}{3} \frac{f_1}{\rho_0 c_0^2} \langle p^2 \rangle - \frac{f_2}{2} \rho_0 \langle \overrightarrow{v}^2 \rangle \right], \tag{2}$$

where the acoustic constant factors are given by $f_1 = 1 - \frac{\rho_0 c_0^2}{\rho_p c_p^2}$ and $f_2 = \frac{2(\rho_p - \rho_0)}{2\rho_p + \rho_0}$, ρ_p and c_p are the density and the speed of sound of the particles, respectively, a is the radius of the suspended particles, $\langle p^2 \rangle$ and $\langle \overrightarrow{v}^2 \rangle$ are, respectively, the mean-square fluctuations of the acoustic pressure and velocity.

The above equations can be used to evaluate the acoustic radiation force from two-dimensional counter-propagating waves in the $x - y$ plane. The waves of the form $p(x,y,t) = 2(1+R)p_0 \left[\cos\left(kx\right) + \cos\left(ky\right) \right] \cos(\omega t)$ will produce a corresponding vector field of the radiation force that is dependent on the wavenumber of the host media, k, as

$$\overrightarrow{F}_{\mathrm{rad}} = V_p \varepsilon \widetilde{p}_0^2 \widetilde{k} \cdot \left[\sin(2\widetilde{k}x) \overrightarrow{e}_x + \sin(2\widetilde{k}y) \overrightarrow{e}_y \right], \tag{3}$$

where abbreviations $V_p = \frac{4}{3}\pi a^3$, $\varepsilon = \frac{(2f_1 + 3f_2)}{8\rho_0 c_0^2}$, and $p_0 = 2p_0(1+R)$ represent the particle volume, the acoustic constant coefficient, and the equivalent excitation pressure amplitude, respectively. R, p_0, and ω are, respectively, the reflection coefficient, the excitation pressure amplitude, and the excitation angular frequency of the matched transducers, $\overrightarrow{e}_x$ and $\overrightarrow{e}_y$ are the unit vectors in the x- and y-directions, respectively. More details of the derivations can be found in the supplementary materials†, Eq. (S6) in section 6.

2.1.2. The attenuation coefficient

With large particles (Mie regime) suspended in the host media, the acoustic energy of the traveling waves could be scattered in other directions [28,31]. The acoustic intensity is attenuated, giving an attenuation coefficient, α, to form a complex wavenumber $\widetilde{k} = k + \alpha i$, where $k = \omega/c_0$.

The attenuation coefficient is [32]

$$\alpha \approx -\frac{\langle \partial_r I \rangle}{2 \langle I_0 \rangle}, \tag{4}$$

where abbreviation ∂_r represents $\frac{\partial}{\partial r}$ along the wave propagating direction $\overrightarrow{e}_r$. $\langle I_0 \rangle = \frac{1}{2} \frac{p_0^2}{\rho_0 c_0}$ means the time-averaged acoustic intensity over a period of the incident wave. The differentiation of the acoustic intensity is given by a linear superposition of the scattering power, $\langle \Im_{sc} \rangle$, as

$$\langle \partial_r I \rangle \approx -\langle \Im_{sc} \rangle \cdot D_n, \tag{5}$$

where the superposition factor D_n is defined as the number of the system Ω involved in the unit cubic meter space.

As shown by the schematic diagram of Fig. 1, a plane wave interacts with a multi-particle system Ω. The acoustic energy taken away by the scattered waves can be computed as (cf. supplementary materials†, Eq. (S24) in section 8, and [33])

$$\langle \Im_{sc} \rangle = -\frac{\rho_0 \omega^2}{2c_0} \mathrm{Re} \left[\int_{\partial\Omega} \widehat{\phi}_{sc} \cdot \widehat{\phi}_{sc}^* \mathrm{dS} \right], \tag{6}$$
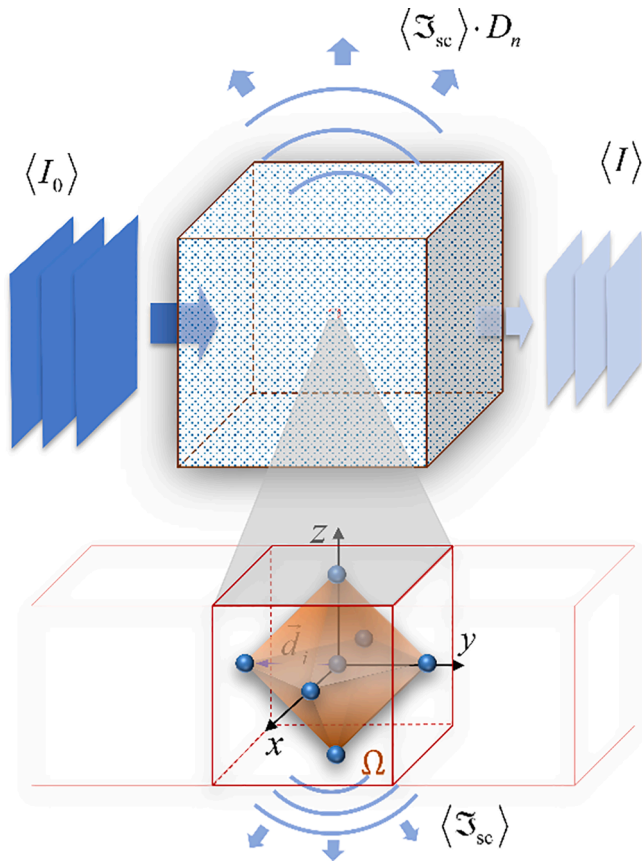
Fig. 1. The acoustic energy flows and the geometry of the multi-particle system Ω. Part of the acoustic energy of the incident wave is transferred to the scattered power $\langle \mathfrak{I}_{sc} \rangle \cdot D_n$, where D_n is the total number of the scattered systems inside a unit cubic meter space. The inset illustrates the schematic geometry of a scattered system (Ω). The central particle is labeled as $i = 1$ and is located at the origin, and the positions of other particles are given as $\vec{d}_i, i = 2, 3, \cdots, 7$.

where superscript * means conjugate, and $\hat{\phi}_{sc}$ is the scattering potential amplitude given in Eq. (S19) of the supplementary materials†, section 7. Then, Eq. (6) becomes

$$\langle \mathfrak{I}_{sc} \rangle = \frac{p_0^2}{2\rho_0 c_0} \frac{1}{k^2} \sum_{n,m} At_{nm} \cdot At_{nm}^*, \tag{7}$$

where the scattering dissipation coefficients $At_{nm} = \sum_{i=1}^{N} \sum_{\nu,\mu} s_{\nu\mu,i} S_{\nu,n}^{\mu,m(1)} \left(\vec{d}_i \right)$. Constant N is the number of particles involved in the system Ω, and the expansion coefficients $s_{\nu\mu,i}$ are defined as the scattering coefficient determined by Eq. (S18), $S_{\nu,n}^{\mu,m(1)} \left(\vec{d}_i \right)$ represents the separation transform matrix of the first kind, depending on the given position vectors of the particles [34].

As a result, the attenuation coefficient from the scattering power can be evaluated by

$$\alpha = \frac{D_n}{2k^2} \sum_{n,m} At_{nm} \cdot At_{nm}^*. \tag{8}$$

It is worth mentioning that for the host media with few suspended particles, the position vectors tend to be large, $\vec{d}_i \rightarrow \infty$, except for the 1st particle locating at the origin, $\vec{d}_1 = 0$. Note that $S_{\nu,n}^{\mu,m(1)}(\infty) \rightarrow 0$ and $S_{\nu,n}^{\mu,m(1)}(0) = 0$, while $S_{n,n}^{m,m(1)}(0) = 1$. The scattering dissipation coefficients are reduced to $At_{nm} = s_{nm} = a_{nm} \cdot s_n$, the beam-shape coefficients $a_{nm} = i^n 4\pi Y_n^m(\theta_{in}, \phi_{in})$ and the scalar scattering coefficients are

$s_n = -\frac{j_n'(ka)}{h_n'(ka)}$, where $Y_n^m(\theta_{in}, \phi_{in})$ are the spherical harmonic function of n-th order and m-th degree determined by the direction of the incident plane wave (θ_{in}, ϕ_{in}), $j_n'(ka)$ and $h_n'(ka)$ are the spherical Bessel and Hankel functions of order n at position ka with primes for differentiation (details in Eqs (S8) and (S17)). In this mode, the attenuation coefficient can be approximated as

$$\alpha = \frac{D_n}{2k^2} \sum_{n,m} a_{nm} s_n \cdot (a_{nm} s_n)^*, \tag{9}$$

where the superposition factor D_n here indicates the total number of particles involved in the unit cubic meter space.

It can be proved that sound attenuation from the relaxation processes due to heat transfer, viscosity, and evaporation is relatively small compared to that from the scattering effects. The former factors reach their maximum when $\tau\omega = 1$, where τ is the relaxation time [35,36]. Generally, for the small particles with radii ranging from 0.01 mm to 1 mm, τ varies from 0.001 s to 0.0001 s, meaning that the most effective frequencies are from 160 Hz to 1600 Hz. However, for ultrasound applications, the frequencies are much higher than these frequencies. As a result, we neglect the contributions from the relaxation processes.

2.1.3. The acoustic streaming

Three acoustic forces dominate the movement of the rigid particles, the gradient force from the external waves, the scattering force from scattered waves by surrounding particles, and the Stokes drag force from micro-streaming.

The particles are driven by the radiation force and delayed by the Stokes drag force arising from the acoustic streaming. It should be noted that acoustic streaming could play an essential role in manipulating the movement of microparticles in some special conditions [37]. However, both experimental and theoretical studies showed that, compared with the acoustic radiation force, the Stokes drag force around a particle in a liquid is not particularly vigorous [38,43], except near a solid structure [39,40] or being suspended inside a microchannel [2]. Therefore, ultrasound-induced microstreaming will become predominant in microchannel [40]. Especially for larger particles, the Stokes drag force becomes less dominant [43,44]. Although the Stoke drag force increases linearly with the radii of the suspended particles, the radiation force is proportional to the cube of the radii of the particles. Consequently, in the parameter range of interest ($ka > 0.1$), especially when the scattering phenomena become significant (ka 1), we can ignore the contribution from Stokes drag force.

2.2. Device fabrication and operation

2.2.1. The BAW platform and experimental setup

Experiments have been performed in a bulk acoustic wave (BAW) device, consisting of a 3D-printed cavity (White resin V4, Formlabs, Inc.) and two orthogonal pairs of matched transducers. Four affixed matched transducers flank the inner walls of the cuboid cavity. The matched transducers are designed to minimize reflection [26,41], and each of them consists of a 25mm × 4mm × 1mm (APC850, APC International, Ltd.) piezoceramic plate with an alumina-loaded epoxy matching layer (EPO-TEK 301, Epoxy Technology, Inc.) applied to the front face. The schematic diagram and design details are given in the supplementary materials†, Fig. S1 and section 1.

The resonance frequency of the matched transducers is measured and calibrated by a vibration measurement system. The transducers are driven by a continuous sinusoidal signal, and the vibrating frequencies and the physical displacements are captured by the laser vibrometer (NLV-2500, Polytec, Ltd.). These values are then transformed into a continuous sinusoidal voltage signal and visualized by a digital oscilloscope (DS1102E, RIGOL Technologies, Inc.). The schematic diagram of the measuring system and the obtained data are illustrated in the

supplementary materials†, Figs S2 and S3 in section 2. The resonance frequency of the transducers is found to be around 2.04 MHz.

Two orthogonal pairs of matched transducers generate the bulk acoustic waves, and electrical wires are soldered to the electrodes of these transducers. We employ an excitation frequency of 2.04 MHz to drive the transducers. At this frequency, the maximum acoustic pressure is delivered as it is near the resonance frequency of the matched transducers. The four transducers are wired in parallel so that their signals are delivered in phase. The excited continuous sinusoidal signal ($V_{pp} = 1V$) is initially generated by a function generator (AFG3022C, Tektronix, Inc.). Then the input voltages herein refer to the peak-to-peak voltage (V_{pp}) and is amplified by an RF power amplifier (150A100D, Amplifier Research, Corp.) before being supplied to the transducers. The schematic diagram of the experimental arrangement can be found in the supplementary materials†, Fig. S4 and section 3. Different load voltages, V_{pp}, supplied to the transducers can be achieved by changing the power gain percentage, $G\%$, of the amplifier; the measuring data is shown in the supplementary materials†, Fig. S5 and section 4. The relationship of the load voltages supplied to the paralleled transducers and the power gain percentages given by the amplifier follows an approximation expression as

$$V_{pp} = V_0 \times 10^{1.5 \cdot G\%}, \tag{10}$$

where $V_0 \approx 12V$ representing the load voltage on the transducers when the power gain percentage $G\%$ is zero.

We prepared suspensions of positive acoustic contrast particles by spreading polystyrene (PS) particles with different radii ranging from 15 μm to 200 μm uniformly in the deionized water. The total weight percentage, the ratio of the mass of suspended particles to the total mass of the mixture, for each PS particle size varies from 0.1 wt% to 1.0 wt%. Fig. 3 shows the acoustic patterns at different combinations of the particle sizes and weight percentages under two orthogonal standing acoustic waves (about 30 s, 2.04 MHz, 50 $G\%$). There are a total of twenty-two suspension samples for the experiments.

2.2.2. Working mechanism

The BAW platform is diagramed in Fig. 2a, and there are four traveling waves generated from the matched transducers. The radiation force results from the Gor'kov potential, which is proportional to the square of the pressure amplitude (Eq. (3)). Small particles are clustered at the Gor'kov potential wells and form the dot patterns under the BAW platform (Fig. 2b and Fig. 3 of small particles). For large particles, part of the acoustic energy of the incident traveling waves is transferred into the scattering wave by reflection, thereby weakening the pressure amplitude along the wave propagating direction. Consequently, the radiation force drives the particles toward the low-pressure region and agglomerate in the central domain (Fig. 2c and Fig. 3 of large particles and high weight percentages).

It is worth noting that this transfer process does not involve any acoustic energy transformation. The acoustic energy taken away by scattering waves is mainly absorbed by the matching layers, which is designed to work at its resonance frequency to minimize the wave reflection and maximize the acoustic energy absorption, i.e., reduce the reflection coefficient R (the supplementary materials†, section 1).

The well-defined patterns are heavily dependent on the uniform Gor'kov potential (Fig. 2a) under the premise that the scattering phenomena from the particles or clusters are negligible. By contrast, the central agglomerating counterpart requires that the acoustic energy be taken away by scattered waves. We need to find out the boundaries that distinguish these two features.

The attenuation coefficient of a traveling wave is evaluated by Eq. (8) when the wave propagates through the suspension (insoluble particles immersed in water) with different weight percentages and size parameters. The theoretical calculation of the attenuation coefficient is validated with experimental data of [28,31]. The dependence of the attenuation coefficient (α) on the size parameter (ka) for the suspension is indicated in Fig. 2d. It can be found that the trends and values of the attenuation coefficient at different weight percentages predicted by our method are basically in good agreement with those from experiments.

The necessary condition of the particles trapped in the central domain is that the square of the pressure amplitude in the central domain is smaller than that outside. Here, we define that the critical condition is reached when the square of the pressure amplitude in the central domain is attenuated by at least half. The width of the BAW platform is 25 mm, and the critical attenuation coefficient ($\alpha_c \approx 25\mathrm{m}^{-1}$) can be determined from $[\exp(-\alpha_c \times 0.025/2)]^2 = 0.5$. The critical value of attenuation requirement is also marked as a black-dashed horizontal line in Fig. 2d.

As shown in Fig. 2c, although the acoustic energy is taken away by the scattered waves and the potential field converges to the central
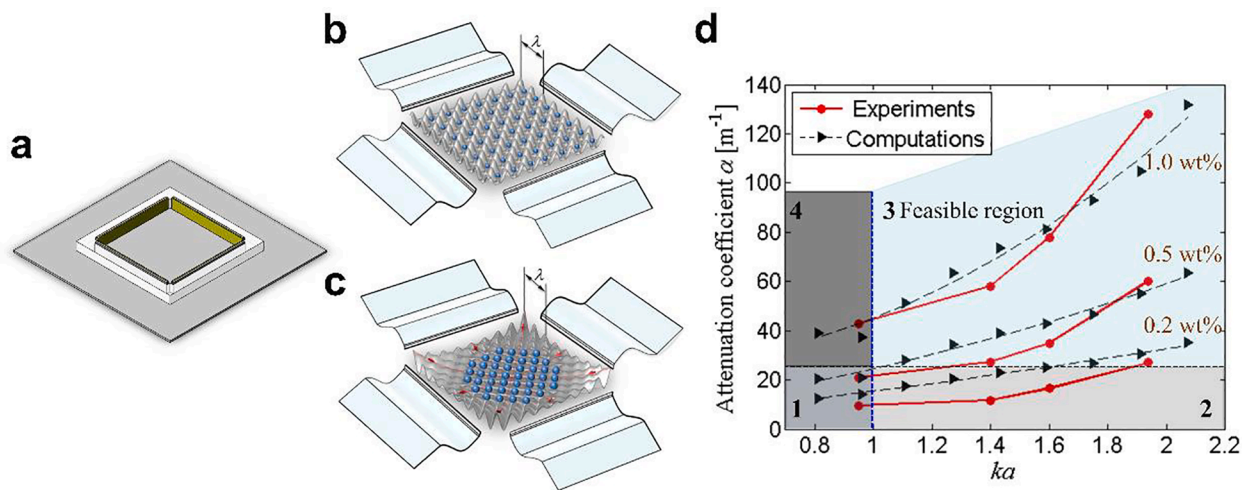

Fig. 2. a A custom-built BAW platform is assembled with four orthogonal matched transducers surrounding a central cavity with a dimension of 25mm × 25mm. The transducers are designed to be driven at their resonance frequency (2.04 MHz) to generate a steeper Gor'kov potential field. **b** The well-defined Gor'kov potential field and **c** the convergent Gor'kov potential field by four traveling waves under the BAW platform. **d** The attenuation coefficient of a traveling plane wave passing through the particle suspension in different weight percentages. The black-dashed curves are quadratic polynomial fitting of prediction results by Eq. (8) (the black triangles), and the red-solid curves are experimental data of [28]. (For interpretation of the references to color in this figure legend, the reader is referred to the web version of this article.)
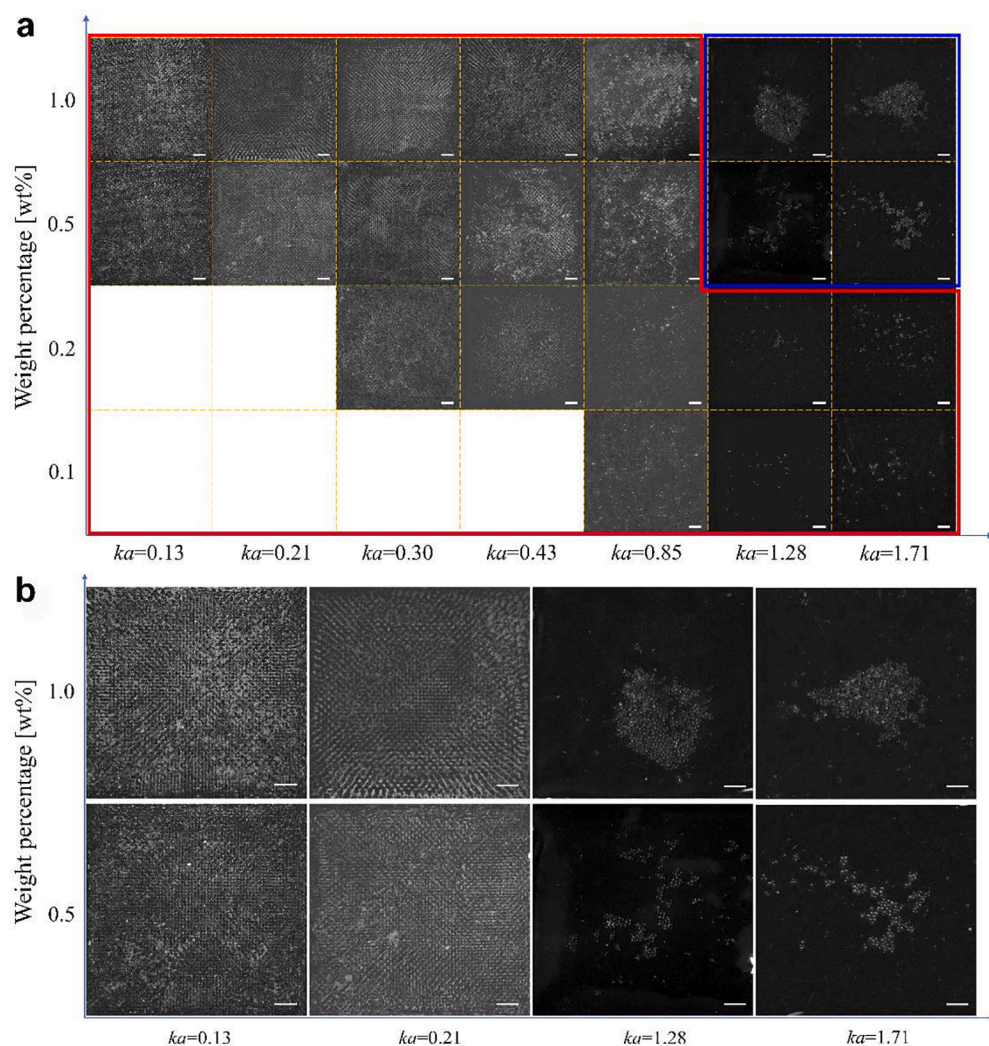
Fig. 3. a Original images of clustered particles in different weight percentages and particle radii under the BAW field. The well-clustered arrays (demonstrated as Fig. 2b) are formed for the scenarios with small particles and/or low weight percentages (images enclosed by red lines). The central agglomerated clusters (demonstrated as Fig. 2c) are presented for the scenarios of large particles and high weight percentages (images enclosed by blue lines). **b** Parts of original images are expanded for clearer visualization. Scale bar = 2.0 mm. (For interpretation of the references to color in this figure legend, the reader is referred to the web version of this article.)

domain, the local minima potential wells could prevent the small particles from escaping the local wells. However, for the large particles ($ka \geq 1$), they are large enough to feel the steep gradient of the potential field. As a result, these particles can pass through the local wells and cluster around the central domain, where the potential field gradient tends to be uniform. The critical value of size requirement is also marked as a blue-dashed vertical line in Fig. 2d.

In short, domain 3 is the feasible region colored by shallow blue in Fig. 2d, where both attenuation and size requirements can be satisfied. Domains 1, 2, and 4 represent low attenuation with small particles, low attenuation with large particles, and high attenuation with small particles, respectively, for the regular grid patterns. Note that the feasible region in Fig. 2d is analyzed under the premise that the boundary condition of the suspended particles is rigid. The feasible region changes for different compressible particles.

2.2.3. Voronoï tessellation analysis

Voronoï tessellation map is famous for analyzing the quality of the particle clusters from the captured particle images [25,27]. Having defined the particle clusters from the Voronoï diagrams, we are able to extract quantitative information, such as the cluster number, particle coordinates, and the proportion of clustered particles. Using these metrics, we can numerically and statistically compare patterning across different experimental conditions.

For better visibility of the particles, the contrast is increased with the removal of background noise in the experimental images using ImageJ software. In order to analyze the patterns of particles, the seeds map of the particles is first identified using ThunderSTORM [42], and the Voronoï tessellation diagrams are generated from the map using SR-Tessler software [29]. The cluster number and proportion of clustered particles can be directly classified and calculated by SR-Tessler software. The proportion of the number of detected clustered particles to the total number of the particles is defined as the cluster ratio, which quantifies the extent of the central agglomeration. More details about the software links and the full process chart of the captured original images to the Voronoï tessellation diagrams can be found in the supplementary materials†, Fig. S6 and section 5.

Note that for small-sized particles ($a < 100\mu m$), the identified seeds map by the software is ineffective and full of noise points, as the captured size of the images (length × width = 20mm × 20mm) is much larger than the size of the particles. Furthermore, the central accumulation of particles appears for the large-sized particles (generally, $a > 100\mu m$) under experimental conditions. We processed the Voronoï tessellation protocol for the particles with a radius larger than 100 μm. However, a systematical analysis of the acoustically-patterning experiments of Rayleigh particles using Voronoï tessellation technique can be found in [27].

3. Results and discussions

We fabricated an acoustic patterning device with four piezo transducers arranged as orthogonal pairs. By driving the piezo transducers at

a frequency close to their primary resonance (2.04 MHz, found in supplementary materials†, Fig. S3 of section 2), we are able to transport the small particles towards the acoustic pressure nodes and large particle towards the central low-pressure domain. We present these clustered populations first, and then apply Voronoï tessellation analysis to quantify the statistic characteristics of the agglomerating products.

3.1. Particle assembly

To investigate this effect, we present the acoustically-forming results inside a 20mm × 20mm region rather than the whole 25mm × 25mm observation window to avoid the acoustic streaming effects around the near-wall regions [44]. The transducers are driven at a 50% power gain percentage (corresponding to a mean load voltage of 68 V_{pp}, referred to Eq. (10) or the supplementary materials†, Fig. S5 of section 4). The size parameter ranges from 0.13 to 1.71, centering around the size requirement ($ka = 1$). The range of weight percentage varies from 0.1 wt% to 1.0 wt%, which centers around 0.5 wt% that is the intersection point of the size and attenuation critical lines (Fig. 2d).

Different experiments are carried out for various combinations of the size parameter and particle concentration. The clustered populations are presented in Fig. 3. Small particles patterning with half-wavelength distance in the fluid under the standing bulk acoustic waves gets trapped to the Gor'kov potential wells. Enclosed by the red line in Fig. 3, the dot or scaffold patterns are formed when using a low concentration of particle suspension, which corresponds to domains 1 and 2 in Fig. 2d. Similarly, the grid patterns are created when using a small particle suspension, which fits domains 1 and 4 in Fig. 2d. We observed that using a higher concentration of small particles does not change the organized patterning arrays but rather the formation of larger sized

clusters at the nodes. On the other hand, when large particles are patterned at high concentrations, the particles are agglomerated in the central domain, as illustrated in Fig. 3 for the scenarios enclosed by blue lines.

Indeed, the capacity to generate uniform and well-defined clusters of acoustic patterns is a valuable characteristic, which has been used to exert control over spheroid culture and organoid tissue engineering [22,23]. In other applications, the uniform clusters over the whole acoustic field are not desirable results, such as separating these clusters from their host media. In this case, a convergent Gor'kov potential field due to the scattering effects (Fig. 2c) may be useful to agglomerate the particles fully. For high concentration cases with large particles ($ka > 1$), the particles cannot keep the balance at the nodes for the well-defined patterns. The convergent Gor'kov potential field leads the particle towards the central domain. Note that the particles tend to cluster at the pressure nodes for a low concentration case, as the acoustic energy does not be transferred considerably. Consequently, the gradient of adjacent peaks in the convergent field is not steep enough to drive the particle to leave the nodes.

We next investigated how Voronoï tessellation maps could be used to characterize the quality of the particle agglomerations. We use the cluster ratio to describe the extent of particle agglomerations. A process chart to obtain the tessellation diagram and the cluster ratio could be found in the supplementary materials†, Fig. S6 of section 5.

A convergent pressure amplitude due to acoustic attenuation appeared to agglomerate the clusters to the central domain. A higher cluster ratio means a greater extent of agglomeration (Fig. 4a). It is found that the cluster ratio will increase for higher weight percentages and the size parameters. The distributions of the particle coordinates show that clusters are mainly located at the central domain. More than
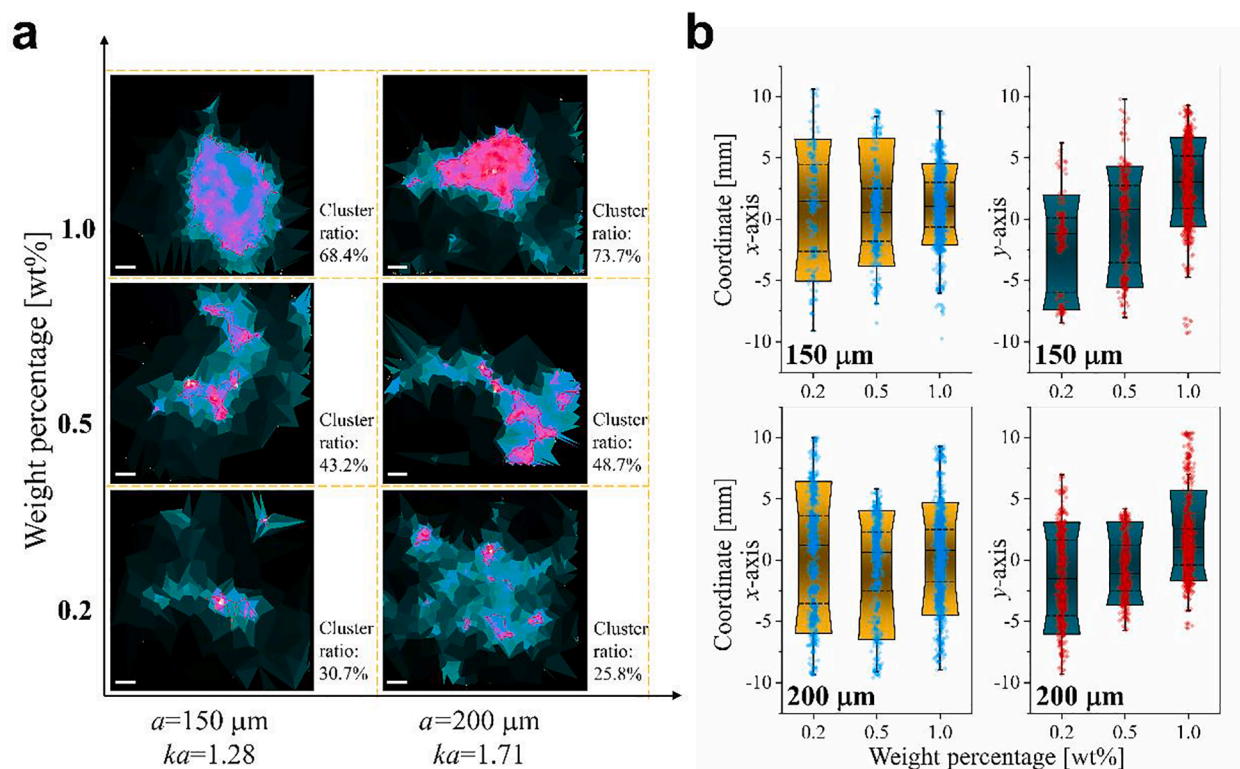

Fig. 4. Voronoï tessellation analysis of clusters agglomerated in different weight percentages and size parameters. **a** The Voronoï tessellation maps are visualized based on the identified particle seeds to construct the particle clusters. The domain with hotter color indicating the density of the particles is higher. The red curves enclose the identified particle clusters (density factor set as 2 in SR-Tessler software). Scale bar = 2.0 mm. **b** Quantitative assessment of the particle clustered positions at different weight percentages and size parameters. In higher weight percentages and larger size parameters, the cluster ratios tend to be higher as well as the coordinates of particles tend to locate at the central domain of the BAW platform. The identified particle coordinates are plotted with the mean, interquartile range, 10% percentile range and 95% confidence intervals. (For interpretation of the references to color in this figure legend, the reader is referred to the web version of this article.)

80% of particles are located within the central 10mm × 10mm domain for 1.0 wt% at particle radii of both 150 μm and 200 μm with cluster ratios of 68.4% and 73.7%, respectively. By contrast, the particles are relatively dispersedly distributed in the whole 20mm × 20mm region for the cases with lower weight percentages.

The above analysis reveals a strong association of clustered quality with the weight percentage and the size parameter. These results imply that the dispersed clusters can be gathered with improved weight percentage, while this phenomenon is not so evident with the increase of the size parameter.

3.2. Spatial quantification of central agglomeration

In order to conclude the results statistically, we repeat the experiments five times across a range of weight percentages for the particle radii at 100 μm, 150 μm, and 200 μm. The cluster ratio is used as an index to distinguish the clustered results. We define that if the cluster ratio is greater than 50%, the particles are well agglomerated, marked as a blue triangle. Otherwise, the quality of agglomeration is lacking, which is marked as a red circle. The statistic chart is given in Fig. 5.

There is a critical range where the cluster ratio fluctuates around 50%. The critical range is contained between the high wt boundary and the low wt boundary. The high wt boundary is defined as a curve that connects the experimental conditions among large particles ($ka > 1$) with only a cluster ratio smaller than 50%. By contrast, the low wt boundary is a curve that corresponds to the conditions starting to appear a cluster ratio greater than 50%. The linear interpolation is applied to estimate the number of the cluster ratio that is smaller than 50% for every specific particle radius. The interpolating points are marked as black dots. Considering the above description, we formulate the high and low wt boundaries as

$$\begin{cases} h_{wt\%} = -0.6977 \cdot ka + 1.6930 \\ l_{wt\%} = -0.1744 \cdot ka + 0.5733 \end{cases} \tag{11}$$

where ka represents the size parameter of the suspended particles. Dependent variables $h_{wt\%}$ and $l_{wt\%}$ describe the distribution of weight percentages for high (visualized by the dark blue line) and low (the dark brown line) wt curves, respectively.

More generally, these boundaries imply that in the domain above the high wt boundary, the cluster ratio should be greater than 50%, while that below the low wt boundary is smaller than 50% statistically. This route provides a means to quantifiably determine the weight percentage and size parameter limits for particle agglomeration. It is worth mentioning that the boundary evaluation is consistent with the size and
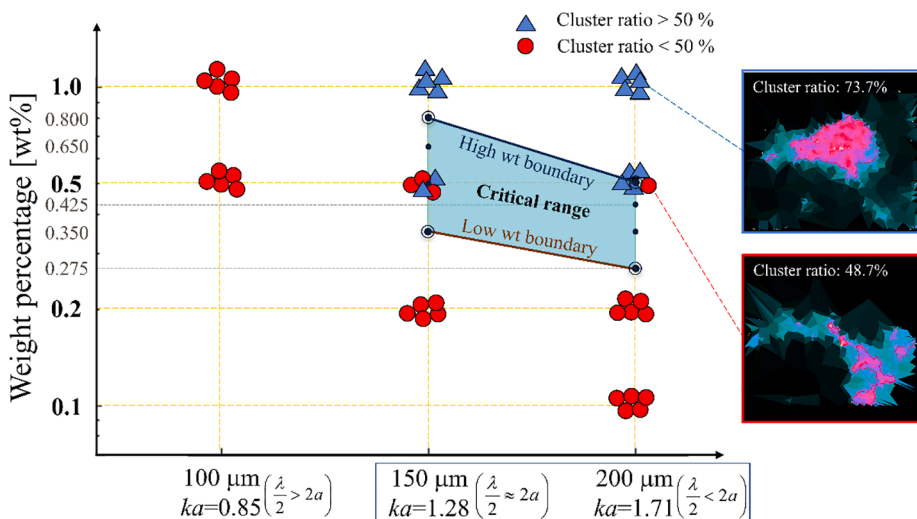
attenuation requirements in the semi-analytical approximation shown in Fig. 2d. These results also highlight the requirements for particle agglomeration applications.

3.3. Cluster number at different load power gain

We used a laser vibrometer mounted on a motorized stage to map the load voltages generated by a 2.04 MHz matched transducer at different power gain percentages (10 G% to 60 G%). Unsurprisingly, the devices driven with higher power gain percentages produced vibration with higher load voltage (Eq. (10) and supplementary materials†, Fig. S5 of section 4). For power gain percentages higher than 60 G%, the transducers work irregularly and lose their mapping relationship between the power gain percentage and the load voltage.

We repeat the experiments five times for the particle radii of 150 μm and 200 μm and the weight percentages at 0.5 wt% and 1.0 wt%. The corresponding statistical data of cluster number and cluster ratio tends towards stability, with the power gain percentage increasing from 20G% to 60G%, as shown in Fig. 6. The identified cluster number and related trends of mean values are highlighted by the red colors, while the shallow blue boxes and lines visualize the interquartile range with 95% confidence intervals and corresponding variations of mean values of the cluster ratio.

As mentioned before, a convergent Gor'kov potential field (Fig. 2c) is formed by adequately introducing acoustic attenuation. The higher load voltages produce steeper pressure gradients. Consequently, the increased acoustic force makes the particles agglomerate towards the central domain more effectively. As expected, the higher the power gain percentages load to the transducers, the tighter the central agglomeration distributions. Specifically, the cluster ratio is attributed to the fact that a small power gain percentage (i.e., the load voltage, supplementary materials†, Fig. S5 of section 4 and Eq. (10)) produces loosely agglomeration results compared with the tight products formed at high power gain percentages. Moreover, higher power gain percentages tend to make fewer cluster numbers.

Although an acoustic force will be exerted in all field-exposed systems, this analysis showed that the power gain percentage/load voltage must exceed a specific threshold limit (such as 40G% or 48 V_{pp} for 0.5 wt %, and 50G% or 68 V_{pp} for 1.0 wt%). In this case, we can produce pressure gradients capable of generating desirable central productions with a cluster ratio greater than 50%, and the averaged number of clusters converges to one.
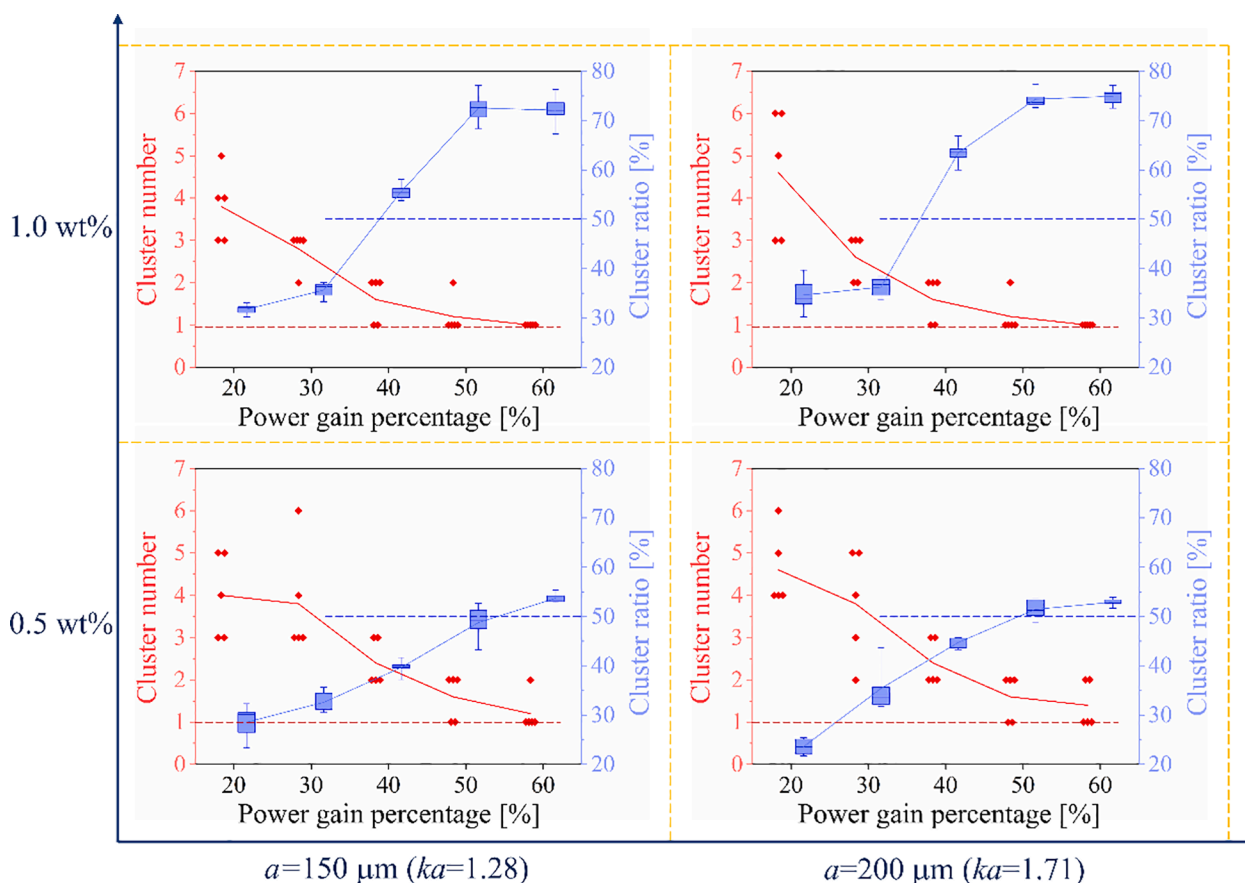

Fig. 5. Statistic analysis of clusters agglomerated in different weight percentages and size parameters. Data is collected from five separate images per group. Each red circle or blue triangle represents a quantitative assessment by Voronoï tessellation analysis of the corresponding experimental image. There is a critical range to distinguish the central agglomeration results (Cluster ratio greater than 50%) and the nodes clustered samples (Cluster ratio < 50%). In this range, a higher size parameter tends to map a smaller weight percentage. (For interpretation of the references to color in this figure legend, the reader is referred to the web version of this article.)

Fig. 6. Quantitative and statistic assessment of clusters agglomerated in different weight percentages and size parameters across a range of power gain percentage. Voronoï tessellation is used to quantify the cluster ratio and the cluster number for every experimental image. In higher power gain percentage/load voltage fields, the cluster numbers tend towards one (red-dashed lines), which indicates that most of the particles are agglomerated together. Meanwhile, the cluster ratio tends towards stability (blue-dashed lines) after 40–50 G%. Data is collected from five separate images per group. (For interpretation of the references to color in this figure legend, the reader is referred to the web version of this article.)

4. Conclusions

We have demonstrated a BAW platform that is capable of agglomerating PS particles, which breaks the saturation limit of the size of acoustic pressure nodes. Considering the acoustic energy being taken away by the complex scattering phenomena of suspended particles and partly absorbed by the surrounding matching layers, a convergent Gor'kov potential field is created, and the corresponding acoustic radiation force propels the particles. We derived the acoustic radiation force and further proposed a computational model for the attenuation coefficient due to the scattering effect. We presented the parametric space that determines the particles either clustered into the pressure nodes for uniform particle arrays or agglomerated together for layer structures. We demonstrated how to get rid of grid patterns of a BAW platform by increasing the suspended particle size and concentration. In contrast, by reducing the particle size or particle concentration, the well-defined clustered arrays appear. In this mode, the parametric space could be thought of as a criterion to guide the developmental pathways of the acoustically formed populations. These parametric thresholds have been explored and verified by a series of acoustically-patterning experiments.

Moreover, we have employed a sophisticated Voronoï tessellation method to analyze the experimental images and numerically and statistically quantify acoustically formed particle clusters. Specifically, quantitative metrics, including cluster number, particle coordinates, and cluster ratio, have been extracted to assess the quality of agglomeration layers under different experimental conditions (size parameter, particle concertation, and load voltage). The results have shown that particles are able to concentrate in the central domain. Further increase in the load voltage improves the extent of the agglomeration products.

We argue that the methods and principles in the current study hold great potential in tissue engineering, bioprinting, micro-object assembly, and material fabrication.

Declaration of Competing Interest

The authors declare that they have no known competing financial interests or personal relationships that could have appeared to influence the work reported in this paper.

Appendix A. Supplementary data

Supplementary data to this article can be found online at https://doi.org/10.1016/j.ultsonch.2021.105590.

References

[1] G. Destgeer, B.H. Ha, J.H. Jung, H.J. Sung, Jin Ho Jung, and Hyung Jin Sung. Submicron separation of microspheres via travelling surface acoustic waves, Lab Chip 14 (24) (2014) 4665–4672.

[2] Wu Mengxi, Yingshi Ouyang, Zeyu Wang, Rui Zhang, Po-Hsun Huang, Chuyi Chen, Hui Li, Peng Li, David Quinn, Ming Dao, et al., Isolation of exosomes from whole blood by integrating acoustics and microfluidics, Proc. Natl. Acad. Sci. 114 (40) (2017) 10584–10589.

[3] D. Foresti, K.T. Kroll, R. Amissah, F. Sillani, K.A. Homan, D. Poulikakos, J.A. Lewis, Acoustophoretic printing, Sci. Adv. 4 (8) (2018) eaat1659, https://doi.org/10.1126/sciadv.aat1659.

[4] V. Vyas, M. Lemieux, D.A. Knecht, O.V. Kolosov, B.D. Huey, Microacoustic-trap (at) for microparticle assembly in 3d, Ultrason. Sonochem. 57 (2019) 193–202.

[5] K. Melde, A.G. Mark, T. Qiu, P. Fischer, Andrew G. Mark, Tian Qiu, Peer Fischer, Holograms for acoustics, Nature 537 (7621) (2016) 518–522.

[6] Y. Zhu, H.u. Jie, X. Fan, J. Yang, B. Liang, X. Zhu, J. Cheng, Fine manipulation of sound via lossy metamaterials with independent and arbitrary reflection amplitude and phase, Nat. Commun. 9 (1) (2018) 1–9.

[7] Z. Ma, A.W. Holle, K. Melde, T. Qiu, K. Poeppel, V.M. Kadiri, P. Fischer, Acoustic holographic cell patterning in a biocompatible hydrogel, Adv. Mater. 32 (4) (2020) 1904181.

[8] M. Wang, L.e. He, Y. Yin, Magnetic field guided colloidal assembly, Mater. Today 16 (4) (2013) 110–116.

[9] O.M. Maragò, P.H. Jones, P.G. Gucciardi, G. Volpe, A.C. Ferrari, Optical trapping and manipulation of nanostructures, Nat. Nanotechnol. 8 (11) (2013) 807–819.

[10] D. Choudhary, A. Mossa, M. Jadhav, C. Cecconi, Bio-molecular applications of recent developments in optical tweezers, Biomolecules 9 (1) (2019) 23.

[11] B.W. Drinkwater, Dynamic-field devices for the ultrasonic manipulation of microparticles, Lab Chip 16 (13) (2016) 2360–2375.

[12] Adem Ozcelik, Joseph Rufo, Feng Guo, Gu Yuyang, Peng Li, James Lata, Tony Jun Huang, Acoustic tweezers for the life sciences, Nat. Methods 15 (12) (2018) 1021–1028.

[13] J. Greenhall, F. Guevara Vasquez, B. Raeymaekers, Ultrasound directed self-assembly of user-specified patterns of nanoparticles dispersed in a fluid medium, Appl. Phys. Lett. 108 (10) (2016) 103103, https://doi.org/10.1063/1.4943634.

[14] Zhenhua Tian, Shujie Yang, Po-Hsun Huang, Zeyu Wang, Peiran Zhang, Gu Yuyang, Hunter Bachman, Chuyi Chen, Wu Mengxi, Yangbo Xie, et al., Wave number–spiral acoustic tweezers for dynamic and reconfigurable manipulation of particles and cells, Sci. Adv. 5 (5) (2019) eaau6062.

[15] Zewei Hou, Zhitao Zhou, Peng Liu, Yongmao Pei, Deformable oscillation of particles patterning by parametric bulk acoustic waves, Extreme Mech. Lett. (2020) 100716.

[16] L. Rayleigh, On the momentum and pressure of gaseous vibrations, and on the connection with the virial theorem, Phil. Mag. 3 (1902) 338–346.

[17] Lev Petrovich Gor'kov, On the forces acting on a small particle in an acoustical field in an ideal fluid, Sov. Phys. Dokl. 6 (1962) page 773.

[18] C.E. Owens, C.W. Shields, D.F. Cruz, P. Charbonneau, G.P. López, Highly parallel acoustic assembly of microparticles into well-ordered colloidal crystallites, Soft Matter 12 (3) (2016) 717–728.

[19] Carlos Mario Giraldo Atehortúa, Nicolás Pérez, Marco Aurelio Brizzotti Andrade, Luiz Octávio Vieira Pereira, Julio Cezar Adamowski, Water-in-oil emulsions separation using an ultrasonic standing wave coalescence chamber, Ultrason. Sonochem. 57 (2019) 57–61.

[20] Sixing Li, Feng Guo, Yuchao Chen, Xiaoyun Ding, Peng Li, Lin Wang, Craig E. Cameron, Tony Jun Huang, Standing surface acoustic wave based cell coculture, Anal. Chem. 86 (19) (2014) 9853–9859.

[21] D.J. Collins, B. Morahan, J. Garcia-Bustos, C. Doerig, M. Plebanski, A. Neild, Two-dimensional single-cell patterning with one cell per well driven by surface acoustic waves, Nat. Commun. 6 (1) (2015) 1–11.

[22] S. Li, P. Glynne-Jones, O.G. Andriotis, K.Y. Ching, U.S. Jonnalagadda, R.O. C. Oreffo, M. Hill, R.S. Tare, Application of an acoustofluidic perfusion bioreactor for cartilage tissue engineering, Lab Chip 14 (23) (2014) 4475–4485.

[23] James P.K. Armstrong, Jennifer L. Puetzer, Andrea Serio, Anne Géraldine Guex, Michaella Kapnisi, Alexandre Breant, Yifan Zong, Valentine Assal, Stacey C. Skaalure, Oisín King, et al., Engineering anisotropic muscle tissue using acoustic cell patterning, Adv. Mater. 30 (43) (2018) 1802649.

[24] M. Akella, J.J. Juárez, High-throughput acoustofluidic self-assembly of colloidal crystals, ACS Omega 3 (2) (2018) 1425–1436.

[25] Ghulam Destgeer, Ali Hashmi, Jinsoo Park, Husnain Ahmed, Muhammad Afzal, Hyung Jin Sung, Microparticle self-assembly induced by travelling surface acoustic waves, RSC Adv. 9 (14) (2019) 7916–7921.

[26] Charles R.P. Courtney, C.-K. Ong, B.W. Drinkwater, A.L. Bernassau, P.D. Wilcox, D. R.S. Cumming, Manipulation of particles in two dimensions using phase controllable ultrasonic standing waves, Proc. Royal Soc. A: Math. Phys. Eng. Sci. 468 (2138) (2012) 337–360.

[27] J.P.K. Armstrong, S.A. Maynard, I.J. Pence, A.C. Franklin, B.W. Drinkwater, M. M. Stevens, Spatiotemporal quantification of acoustic cell patterning using voronoï tessellation, Lab Chip 19 (4) (2019) 562–573.

[28] V.J. Stakutis, R.W. Morse, M. Dill, R.T. Beyer, Attenuation of ultrasound in aqueous suspensions, J. Acoust. Soc. Am. 27 (3) (1955) 539–546.

[29] F. Levet, E. Hosy, A. Kechkar, C. Butler, A. Beghin, D. Choquet, J.-B. Sibarita, Sr-tesseler: a method to segment and quantify localization-based superresolution microscopy data, Nat. Methods 12 (11) (2015) 1065–1071.

[30] H. Bruus, Acoustofluidics 7: The acoustic radiation force on small particles, Lab Chip 12 (6) (2012) 1014–1021.

[31] J.R. Allegra, S.A. Hawley, Attenuation of sound in suspensions and emulsions: Theory and experiments, J. Acoust. Soc. Am. 51 (5B) (1972) 1545–1564.

[32] Allan D. Pierce, Robert T. Beyer, Acoustics: An introduction to its physical principles and applications. 1989 Edition, Acoustical Society of America, 1990.

[33] T. Tang, L. Huang, Mie particle assembly by a converging ultrasound field and acoustic interaction forces, Appl. Acoust. 180 (2021) 108123, https://doi.org/10.1016/j.apacoust.2021.108123.

[34] P.A. Martin, Multiple Scattering: Interaction Of Time-Harmonic Waves with N Obstacles, Cambridge University Press, 2006.

[35] F.E. Marble, Some gasdynamic problems in the flow of condensing vapors, Astronaut. Acta 14 (1969) 585–613.

[36] G.A. Davidson, Sound propagation in fogs, J. Atmos. Sci. 32 (11) (1975) 2201–2205.

[37] P.B. Muller, H. Bruus, Theoretical study of time-dependent, ultrasoundinduced acoustic streaming in microchannels, Phys. Rev. E 92 (6) (2015), https://doi.org/10.1103/PhysRevE.92.063018.

[38] D.L. Miller, Particle gathering and microstreaming near ultrasonically activated gas-filled micropores, J. Acoust. Soc. Am. 84 (4) (1988) 1378–1387.

[39] W.L. Nyborg, Acoustic streaming near a boundary, J. Acoust. Soc. Am. 30 (4) (1958) 329–339.

[40] Daniel Ahmed, Adem Ozcelik, Nagagireesh Bojanala, Nitesh Nama, Awani Upadhyay, Yuchao Chen, Wendy Hanna-Rose, Tony Jun Huang, Rotational manipulation of single cells and organisms using acoustic waves, Nat. Commun. 7 (1) (2016) 1–11.

[41] H. Wang, T. Ritter, W. Cao, K. Kirk, Shung., High frequency properties of passive materials for ultrasonic transducers, IEEE Trans. Ultrason. Ferroelectr. Freq. Control 48 (1) (2001) 78–84.

[42] Martin Ovesný, Pavel Křížek, Josef Borkovec, Zdeněk Švindrych, Guy M Hagen, Thunderstorm: a comprehensive imagej plug-in for palm and storm data analysis and super-resolution imaging, Bioinformatics 30 (16) (2014) 2389–2390.

[43] S. Melker Hagsater, T. Glasdam Jensen, Henrik Bruus, Jorg Peter Kutter, Acoustic resonances in microfluidic chips: full-image micro-PIV experiments and numerical simulations, Lab Chip 7 (10) (2007) 1336–1344.

[44] Peter Barkholt Muller, Rune Barnkob, Mads Jakob Herring Jensen, Henrik Bruus, A numerical study of microparticle acoustophoresis driven by acoustic radiation forces and streaming-induced drag forces, Lab Chip 12 (22) (2012) 4617–4627.